journal

J. Am. Ceram. Soc., 92 [2] 491–500 (2009)
DOI: 10.1111/j.1551-2916.2008.02887.x

Process-Controlled Plasma-Sprayed Yttria-Stabilized Zirconia Coatings: New Insights from Ultrasmall-Angle X-ray Scattering

Yaping Li,* Weiguang Chi, Sanjay Sampath,* Allen Goland, and Herbert Herman*,**,†

Department of Materials Science and Engineering, State University of New York at Stony Brook, Stony Brook, New York 11794-2275

Andrew J. Allen*

Ceramics Division, National Institute of Standards and Technology, Gaithersburg, Maryland 20899

Jan Ilavsky*

Advanced Photon Source, Argonne National Laboratory, Argonne, Illinois 60439

A multicomponent microstructure model is applied in ultrasmall-angle X-ray scattering studies of two groups of plasma-sprayed yttria-stabilized zirconia thermal barrier coatings (TBCs). One group was sprayed from a single powder feedstock using controlled processing conditions. The other group included three different feedstock morphologies (obtained from different manufacturing methods), each with a similar particle size distribution and sprayed under the same average controlled processing conditions. The microstructure is quantitatively related to the feedstock morphology and processing conditions. Relationships are explored among these microstructures and the coating properties (e.g., thermal conductivity, elastic modulus). The degree of microstructural anisotropy is demonstrated to be pore-size dependent, being more pronounced for larger pores, and more sensitive to feedstock morphology (*powder processing*) than to spray processing. The microstructure analysis indicates two broad distributions of interlamellar pores, which combined, account for 70%–80% of the pore volume. The total porosity is found to increase with decreasing particle temperature or velocity. For all coatings, a negative linear relationship exists between thermal conductivity and total porosity. Comparison of the new analysis is made with earlier small-angle neutron scattering results, and implications are considered for a more general application of this metrology in TBC microstructure design.

I. Introduction

THERMAL barrier coatings (TBCs) produced by thermal spraying (principally, plasma spraying) have been widely used for industrial applications such as in gas turbines and diesel engines.[1–3] The performance of these ceramic coatings in operation at high temperature, in a corrosive atmosphere, and under mechanical loading depends largely on their microstructure, and particularly on the distribution of both the solid/gas and solid/solid interfaces. Furthermore, it is the anisotropic distribution of pores, cracks, and interfaces that govern the thermal and mechanical properties of the coatings.[4] Thus, achieving a quantitative understanding of these complex microstructures in plasma-sprayed TBCs is critical to developing the advanced materials and technologies that will lead to superior high-temperature performance. This demands a quantitative characterization of microstructural parameters such as the component volume fractions and the size, shape, and orientation distributions of the void networks.

Previously, different kinds of small-angle X-ray and neutron scattering measurements (SAXS and SANS) have demonstrated the ability to provide the necessary quantitative microstructural characterization.[5–8] These diffraction-based methods have been used to successfully extract statistically representative microstructural information important for developing advanced technological materials. Taking advantage of the penetrating power of neutrons in solid materials, the SANS method first revealed the multicomponent anisotropic microstructures in ceramic plasma-sprayed coatings.[9–12] By exploiting and extending the multiple-SANS (MSANS) technique, it was possible eventually to provide a fully quantitative analysis of the microstructures found in water plasma-sprayed or air plasma-sprayed (APS) TBCs,[13–15] including metallic TBCs,[16] both as a function of the feedstock/process variables[17] and as required for property prediction.[18] SAXS methods have now also been applied to TBC microstructure characterization in order to exploit the small X-ray beam size to study thinner TBCs of greater industrial relevance,[19–21] and a wider range of application[22,23] and type,[24] including electron-beam physical vapor deposits (EB-PVD).[25–27] A more rapid ability to characterize the microstructures of thin APS coatings (here 400 μm, but potentially <100 μm) over the scale range from nanometers to micrometers has emerged from the high spatial resolution (small-beam size) of anisotropic ultrasmall-angle X-ray scattering (USAXS) measurements.[28] Anisotropic USAXS measurements are particularly well suited to quantify, in a single scan, the microstructure over a continuous scale range from nanometers to micrometers for a given sample orientation. This now motivates the quantitative microstructure characterization of a new sample matrix, aimed at relating microstructure to the thermal and mechanical properties for TBC materials of significant current industrial interest. To this end, the present study focuses on the USAXS microstructure characterization of two groups of plasma-sprayed yttria-stabilized zirconia (YSZ) coatings, coupled with a range of processing controls and property measurements. Reported herein are the results of a study based on two *processing maps* and three *powder morphology* samples (designated PRM and POM, respectively), encompassing a large variation of processing conditions and the feedstock morphology.

J. Smialek—contributing editor

Manuscript No. 25012. Received July 22, 2008; approved November 10, 2008.
This research was supported by the National Science Foundation GOALI-FRG Program at the State University of New York at Stony Brook under the Grant No. CMMI 0605704. The use of the Advanced Photon Source was supported by the U.S. Department of Energy, Office of Basic Energy Sciences, under Contract No. DE-AC02-06CH11357.
*Member, The American Ceramic Society.
**Fellow, The American Ceramic Society.
†Author to whom correspondence should be addressed. e-mail: hherman@ms.cc.sunysb.edu

Table I. Feedstock Characteristics and Deposition Parameters

Sample	Powder type	Manufacturer	Particle size (μm) mean, minimum, maximum, d_{50}†	H_2 (SLPM†)	N_2 (SLPM)	Current (A)	Voltage (V)	Temperature (°C)	Velocity (m/s)	Substrate temperature (°C)
PRM-1	F&C	Saint-Gobain Ceramics, Worcestor, MA	64.1, 31.4, 96.9, 64.0	1.7	31.9	466	65.8	2504±10	80±2	290
PRM-2	F&C	Saint-Gobain Ceramics	64.1, 31.4, 96.9, 64.0	12.0	63.1	634	79.5	2677±10	150±2	290
PRM-3	F&C	Saint-Gobain Ceramics	64.1, 31.4, 96.9, 64.0	6.0	31.6	634	69.2	2631±10	103±2	280
PRM-4	F&C	Saint-Gobain Ceramics	64.1, 31.4, 96.9, 64.0	6.0	31.6	466	66.8	2518±10	79±2	280
POM–F&C	F&C	Saint-Gobain Ceramics	64.1, 31.4, 96.9, 64.0	7.1	48.0	466	79.8	2663±10	125±2	NA
POM–HOSP	HOSP	Sulzer Metco	60.8, 27.4, 94.7, 60.4	6.9	51.9	513	79.3	2666±10	125±2	260
POM–A&S	A&S	H. C. Starck, Goslar, Germany	58.7, 26.8, 97.0, 55.0	6.9	51.7	548	76.1	2664±10	125±2	NA

†d_{50} is a value on the distribution such that 50% of the particles have a volume of this value or less. SLPM, standard liters per minute (standard flow); F&C, fused and crushed; A&S, agglomerated and sintered; POM, powder morphology; PRM, processing maps.

The USAXS instrumentation and analysis for effective TBC characterization differs from those used in the SANS and MSANS approach. Previously, a *maximum entropy* algorithm[29] has been applied to determine the apparent size distributions of voids in TBCs from USAXS data associated with different orientations with respect to the substrate plane.[20,26] From such analyses, information was inferred regarding the sizes and volume fractions of the void components. Meanwhile, a more rigorous approach has been developed, presented in a preliminary form,[23] and applied to the analysis of EB-PVD TBCs.[27] The plasma-spray microstructure is somewhat different, and this paper presents the model, for the first time, as it relates to the APS case. The fully quantitative application of this multicomponent anisotropic model has been implemented here for a full sample-set of plasma-sprayed TBCs. Application of the full model has enabled a series of coating microstructures of industrial importance to be interrogated systematically with regard to the generic processing–microstructure–property relations in YSZ-based plasma-sprayed coatings.

Plasma-sprayed coatings are produced by the build-up of molten droplets (*splats*) by successive impact, forming a complex, layered microstructure, with the splats as the fundamental building blocks.[4] Owing to recent advances in process diagnostics, it is now possible to obtain particle characteristics such as temperature, velocity, and size for tens of thousands of particles actually in flight as the coating is deposited. This is providing improved insights into the particles' in-flight state and hence a better understanding of the microstructural characteristics of coatings resulting from various feedstock morphologies and particle size distributions. This diagnostic-integrated process approach to coating characterization, using process maps, leads to a more thorough understanding of the complex multivariable deposition process. In this paper, we demonstrate how the USAXS method can elucidate the complex processing–microstructure–property relationships in plasma-sprayed TBCs and similar systems.

II. Experimental Procedure and Microstructure Model

(1) Coating Preparation

Two groups of YSZ (ZrO_2-8% mass Y_2O_3) coatings were sprayed using a 7 MB torch (Sulzer Metco,‡ Westbury, NY) with N_2–H_2 as the plasma forming gases and N_2 as the carrier gas in ambient atmosphere. The process map or PRM group specimens were produced using a fused-and-crushed (F&C) feedstock, the surface of which has angular polyhedral morphology.[30] The process space was systematically explored with respect to various deposition conditions, with average particle temperatures and velocities ranging from 2500° to 2680°C and 80 to 150 m/s. The powder morphology or POM specimens were produced by spraying three distinctly different feedstock morphologies, namely (1) polyhedral (F&C), (2) solid spherical (agglomerated and sintered, denoted A&S), and (3) hollow spherical (plasma densified or HOSP). All three feedstock morphologies were sprayed such that the average particle temperature and velocity at the center of the plasma plume (averaged over 10 000 particles) were the same without varying the torch parameters significantly. The particle diagnostics were obtained using a in-flight particle sensor DPV-2000 (Tecnar Automation Ltd., St-Bruno, Quebec, Canada), and deposits were made on Al-6061-T6511 substrates of dimension: 225 mm × 25 mm × 3 mm. The selection of substrate type and dimension were due to a larger investigative framework to monitor the curvature of the specimen during and after deposition in an effort to extract linear and nonlinear elastic properties of the coatings. More details can be found in the literature.[31]

Table I provides a list of the process parameters used (feedstock and deposition parameters), together with the resulting particle state for each sample sprayed. For the USAXS measurements, thin coating cross sections (1 mm) were cut perpendicular to the substrate, using an ISOMET 2000 precision diamond-saw (Buehler, Lake Bluff, IL), and ground and polished down to <200 μm using a Tripod Polisher device (Precision TEM Inc., Santa Clara, CA).

(2) USAXS Experiments

Full details of the small-angle scattering method and its application to ceramic systems are given elsewhere.[5,32] When a well-collimated, monochromatic X-ray or neutron beam passes through a heterogeneous material such as a TBC sample, part of the incident beam intensity is scattered out of the incident beam direction by heterogeneities (e.g., voids) within the sample. The scattered intensity profile is essentially a Fourier transform of the real-space microstructure in the direction of the scattering vector, **Q**, which bisects the incident and scattered beam directions. The magnitude of **Q** is given by $Q = |\mathbf{Q}| = (4\pi/\lambda)\sin\theta$, where λ is the X-ray (or neutron) wavelength, and 2θ is the angle of scatter. Because θ is small, the direction of **Q** is approximately in the plane of the sample and is in the azimuthal direction corresponding to the associated scattering direction. In principle, by absolute-calibrating the small-angle scattered intensity, $I(Q)$, as a probability function for scattering out of the incident beam, both the volume fraction (porosity) and the size distribution of the scattering features (voids) can be determined.

Compared with conventional small-angle scattering, where the Q resolution is determined largely by the beam and detector collimation geometry, the ultrasmall-angle scattering method uses multiple crystal Bragg reflections, both before and after the sample, to provide a Q resolution independent of the beam size and determined solely by the inherent angular width of the Bragg reflections. This significantly reduces the minimum accessible Q, and extends the corresponding scale of measurable structural features up into the micrometer regime. In its stan-

‡Certain commercial materials and equipment are identified in this report only to specify adequately the experimental procedure. In no case does such identification imply recommendation by NIST nor does it imply that the material or equipment identified is necessarily the best available for this purpose.

dard form, the scattering data are intrinsically "slit-smeared" in the plane perpendicular to the crystal diffractions in the scattering plane. For studying anisotropic microstructures, crystal diffractions are introduced in the transverse plane before and after the sample, and these remove the slit-smearing effects.

The USAXS experiments were conducted using the NIST-built USAXS instrument[33,34] at XOR-UNI Sector 33-ID at the Advanced Photon Source, Argonne National Laboratory, Argonne, IL, using an X-ray energy of 16.9 keV and a beam size of 0.3 mm × 0.4 mm. This instrument permits examination of the anisotropic microstructure for void sizes up to more than 1 μm.[28] In the present USAXS experiments, the microstructural anisotropy at a number of fixed Q values, corresponding to different length scales, was examined by measuring the scattered intensity while rotating the TBC cross-section sample around the incident beam direction. Thus, the polar angle, α, between the **Q** direction and the symmetry axis, i.e., the spray direction, was varied through 0°–360°. This is denoted an *anisoscan*. Then, the scattered intensity profile was measured as a function of Q at fixed polar angles $\alpha = 0°$, 22.5°, 45°, 67.5°, and 90°, over the Q range from 0.0001 to 0.1 $Å^{-1}$ (a USAXS scan). Because the microstructure is axially symmetric about the spray direction, the three-dimensional microstructure could be obtained by analyzing the one-dimensional scattering data measured in several azimuthal directions.

Raw data were reduced and calibrated, and parasitic background effects removed, using the data reduction software package, Indra.[35] Appropriate multiple scattering corrections were made when needed to the absolute-calibrated scattered intensities, as implemented in the Indra package. The absolute intensity $I(\mathbf{Q})$ data in three directions of **Q** were then simultaneously fitted with a multicomponent structural model, constrained by the additional requirement that the predicted scattering anisotropies are consistent with the *anisocan* data measured at the various Q values.

(3) Anisotropic Model for USAXS Analysis

The complex TBC pore microstructure is divided into three types of voids: interlamellar pores (preferentially oriented parallel with the substrate), intralamellar cracks (preferentially oriented perpendicular to the substrate), and globular pores. A nonlinear least-squares fitting routine is used, which assumes separate Gaussian size distributions of spheroidal void elements with orthogonal radii: R_O, R_O, βR_O, and aspect ratio, β, for each void component. As in previous SANS work,[13–18] reasonable results are obtainable with $\beta = 0.1$, 0.2, and 1.0, respectively, for intralamellar cracks, interlamellar pores, and globular pores. For each void component, j, the scattered intensity, $I_j(Q)$, is given by

$$I_j(Q) = \int_0^\infty \mathrm{d}R_O \int_0^{\pi/2} \mathrm{d}\alpha (P_j(\alpha) I_j^*(QR_O, \beta, X) \sin\alpha) \Phi_j(R_O) \tag{1}$$

where $\Phi_j(R_O)$ is the size distribution and $P_j(\alpha)$ the orientation distribution such that: $\int_0^\infty \Phi_j(R_O)\mathrm{d}R_O = \Phi_{j\mathrm{Total}}$ with $\Phi_{j\mathrm{Total}}$ the j component total porosity and $\int_0^{\pi/2} P_j(\alpha)\sin\alpha\,\mathrm{d}\alpha = 1$.

In the present case, it is convenient to define $P_j(\alpha)$ in the following analytical form, a modified March–Dollase function[36]:

$$P_j(\alpha) = a_0(\{\cos(\alpha - a_1)\}^{a_2} + a_3) \tag{2}$$

where $a_1 = 0°$ for the interlamellar pores and $a_1 = 90°$ for the intralamellar cracks; a_2 determines how narrowly the preferred orientation is associated with the α value given by a_1; with the *larger* values of a_2 defining a *smaller* angular width for the preferred orientation around α_1; a_3 indicates the fraction of the jth component with no preferred orientation, and a_0 is a normalization parameter needed to satisfy the orientation integral requirement given above. The parameters, a_2 and a_3, are adjusted to optimize the fits both to the USAXS data for different **Q** orientations, and to the *anisoscans* obtained at different Q values.

Continuing

$$I_j^*(QR_O, \beta, X) = V_j(R_O)|\Delta\rho|^2 F_j(QR_O, \beta, X) S(Q) \tag{3}$$

where $V_j(R_O) = 4\beta\pi R_O^3/3$, $|\Delta\rho|^2$ is the scattering contrast between the solid phase and the voids, and the structure factor, $S(Q) = 1$, provided that the voids are not significantly correlated with each other. Finally

$$F_j(QR_O, \beta, X) = \frac{9\pi}{2}\left(\frac{J_{3/2}(QR_O K(\beta, X))}{[QR_O K(\beta, X)]^{3/2}}\right)^2 \tag{4}$$

where $J_{3/2}(x)$ denotes a Bessel function of order 3/2 and, for an axially symmetric microstructure:

$$K(\beta, X) = (1 - (1 - \beta^2)X^2)^{1/2}, \quad \text{with } X = \cos\alpha \tag{5}$$

For both sets of interlamellar pores and for the intralamellar cracks, Eqs. (1)–(5) indicate that the scattered intensity, $I_j(Q)$, is largest when **Q** is perpendicular to the planes of these features, i.e., when **Q** is along the βR_O symmetry axis of the individual spheroids. Thus, the small-angle scattering data are most sensitive to the mean opening dimension, $\langle \mathrm{OD} \rangle$, of the planar voids and cracks, given by $\langle \mathrm{OD} \rangle = 4\beta R_O/3$ for the spheroidal elements considered here. General small-angle scattering theory[32] indicates that when $1/Q$ is around half the mean dimension in the direction of **Q**, the data are most indicative of the size and volume fraction of the scattering features. At significantly larger Q ($Q \gg 1/\langle \mathrm{OD} \rangle$), $I_j(Q)$ obeys the Porod scattering law:

$$I_j(Q) = \frac{2\pi|\Delta\rho|^2 S_V^{\mathrm{APP}}}{Q^4} \tag{6}$$

where S_V^{APP} is an apparent void surface area per unit sample volume for the direction of **Q** measured. In fact, as has been described in detail in previous work,[9–14] the orientational dependence of S_V^{APP} amplifies the orientational anisotropy actually present, and this helps distinguish the different void systems in the high Q data. Furthermore, as also shown previously,[8–14] an orientational average of Eq. (6) over all solid angles provides the true surface area, S_V. In the present case, the anisotropic Porod scattering is included in the model described by Eqs. (1)–(5).

Although three types of voids are included in the multicomponent model, it has been found in USAXS studies of plasma-sprayed TBCs that four components must be used to obtain successful fits to the USAXS data while, simultaneously, predicting anisotropies that are consistent with the measured anisoscans.[23] The additional population comprises coarse interlamellar pores, as discussed further below.

(4) Thermal Conductivity Measurements

Thermal conductivity measurements were made in air under ambient conditions at room temperature using a laser-flash instrument (Holometrix Micromet, Holometrix Inc., division of Netzch Inc., Burlington, MA) on 12.7-mm-diameter disk-shaped free-standing specimens. Coatings, typically in the thickness range of 300–400 μm were carefully separated from the aluminum substrate by grinding away the aluminum. The free-standing samples were then sprayed with a thin film of spray on graphite (Balkamp Inc., Indianapolis, IN). Further details of the procedure is reported in earlier papers.[37,38] The measurements were carried out in the out-of-plane (spray) direction, normal to the coating (see Table II). The quoted standard deviation of the measurements is for nine separate measurements for each specimen.

(5) Elastic Modulus Measurement

In order to determine how the microstructural anisotropy is related to the elastic modulus anisotropy, both the in-plane and

Table II. Thermal Conductivity (Out-of-Plane) and Elastic Modulus Measurements

Sample	Thermal conductivity ($W \cdot (m \cdot K)^{-1}$)	E(spray) (GPa) (out-of-plane)	E(plane) (GPa) (in-plane)
PRM-1	0.97 (2)		
PRM-2	1.29 (2)		
PRM-3	1.13 (1)		
PRM-4	1.00 (1)		
POM–F&C	1.30 (1)	55.9 (17)	46.5 (13)
POM–HOSP	1.00 (3)	33.5 (12)	39.4 (16)
POM–A&S	1.18 (14)	51.5 (27)	45.6 (15)

Standard deviation uncertainties given in parentheses in least significant digits. POM, powder morphology; PRM, processing maps.

out-of-plane elastic indentation moduli were measured for the POM samples using an instrumented depth-sensitive microindentation method with the coatings attached to the substrate (Table II). A Fischerscope (Fischer Technology Inc., Windsor, CT) 100°C microhardness tester using a Vickers-type indenter (with a maximum load $F_{max} = 1$ N) was used, with impressions taken at random locations. Each sample was indented at 15 different locations, and the indentation moduli measured for each of the 15 indents. The mean value of the measurements on each sample is presented in Table II, together with the corresponding standard deviation uncertainty for 15 separate measurements for each specimen.

III. Results and Discussion

(1) Microstructural Anisotropy in PRM and POM Coatings

Figure 1 compares scanning electron microscopy (SEM) images with USAXS results presented in a polar plot for a typical plasma-sprayed TBC. It shows the variation in the scattering intensity versus the angle, α, at four different values of Q. The coordinate system used throughout this paper is given in Fig. 1(a). The polar plot shows that the maximum scattering intensity occurs when **Q** is parallel to the spray direction. Here and below, the polar plots need to be interpreted in the context of the plasma-sprayed microstructure. All of the anisotropy in the microstructure arises from the anisotropic orientation distribution of features that are planar or oblate in their shape. There are two main anisotropic distributions: interlamellar pores preferentially aligned parallel to the substrate, and intralamellar cracks preferentially aligned perpendicular to the substrate plane. For a given planar pore or crack, the scattering intensity is at a maximum when **Q** is perpendicular to the plane of the pore.[9,13] Thus, the anisotropic scattering intensity is expected to have a maximum along the spray direction due to the interlamellar pore orientation distribution, and another maximum when **Q** is parallel to the substrate plane due to the intralamellar crack orientation distribution. In practice, this second maximum is much suppressed because (i) the cracks tend to be less prominent than the interlamellar pores, and (ii) the orientation of **Q** parallel to the substrate plane is not just one direction, but represents all directions within the substrate plane. Nevertheless, the second maximum due to the cracks is visible in the polar plot of Fig. 1 for the *anisoscan* data at the highest Q value, corresponding to features with the smallest opening dimension—such as the cracks.

Figure 1(b) illustrates the limited utility of micrographs for quantitative analysis of the coating microstructures, providing significant impetus for the USAXS studies reported here, as well as the earlier SANS work.[9] From Figs. 1 and 2, all of the PRM and POM samples exhibit a similar trend for the Q-dependent patterns. Namely, at small Q, the anisotropic profile of the normalized scattering intensity is an elongated ellipsoid orientated along the 0°–180° spray direction, implying that the interlamellar pores, which are predominantly parallel to the substrate, are the dominant microstructural features in the large pore size regime ($Q = 0.00025$ Å^{-1}, corresponding to $\langle OD \rangle \approx 2/Q = 0.8$ μm).

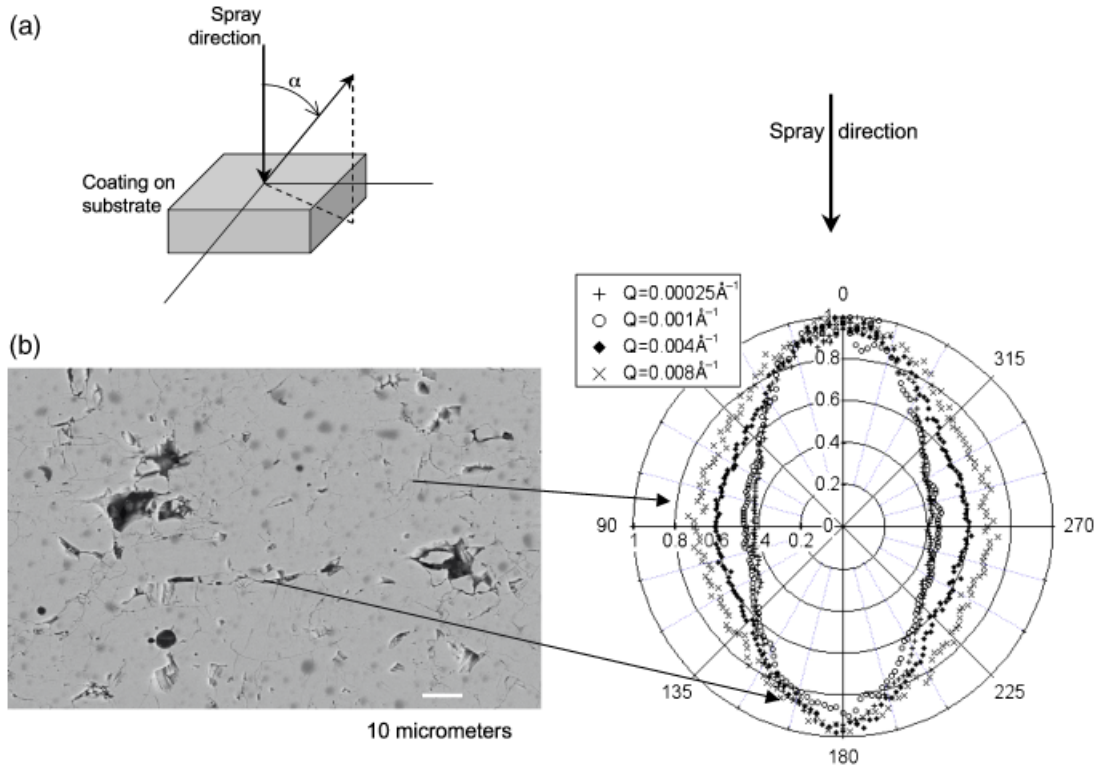

Fig. 1. (a) Schematic of the sample coordinate system used throughout this paper; (b) typical cross-sectional scanning electron micrograph of a thermal barrier coating (TBC); (c) scattering intensity as a function of polar angle, α, at $Q = 0.00025$, 0.001, 0.004, and 0.008 Å^{-1}, respectively, for a typical thermal-sprayed YSZ TBC. Corresponding relationships between the scattering intensity and the microstructural features are schematically illustrated. YSZ, yttria-stabilized zirconia.

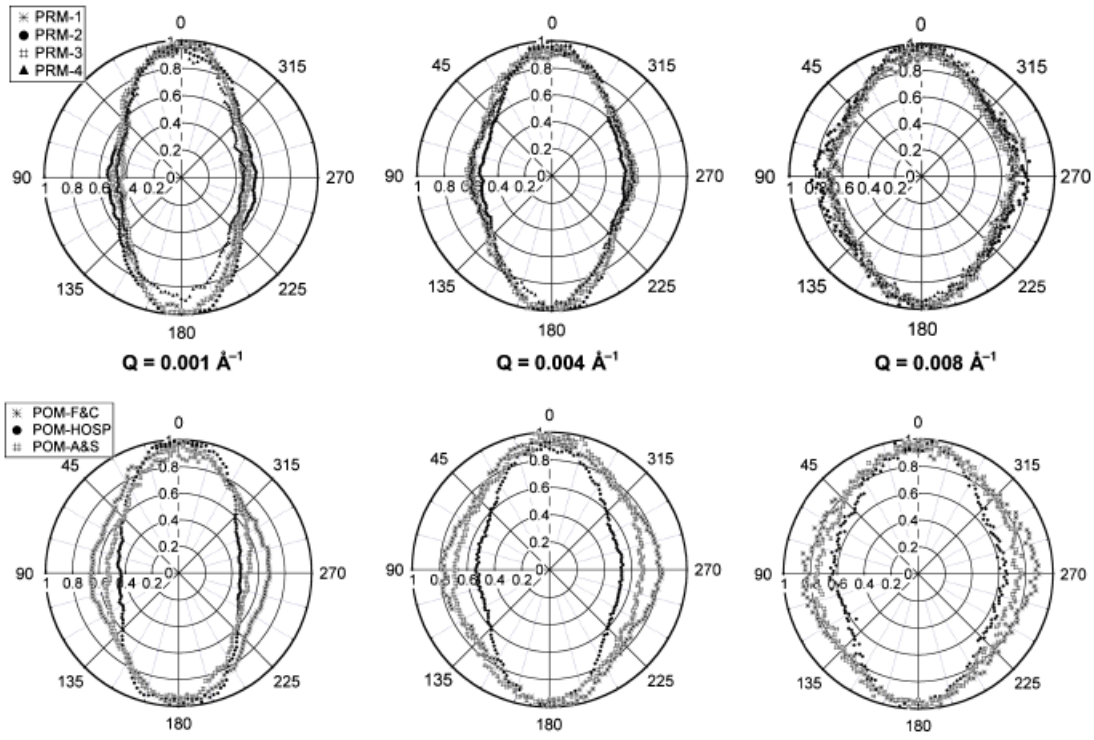

Fig. 2. Scattering intensity as a function of polar angle, α, for PRM coatings (top) and POM coatings (bottom) at $Q = 0.001$, 0.004, and 0.008 Å^{-1}.

However, the relative scattering intensity in the 90°–270° direction (perpendicular to the spray direction) increases at high Q, indicating that the population of intralamellar cracks, which are preferentially perpendicular to the substrate, contribute more to the porosity in the fine pore size regime. Certainly, this is the case for Q up to ≈ 0.004 Å^{-1} (corresponding to $\langle \mathrm{OD} \rangle \approx 2/Q = 50$ nm for the fine cracks). For $Q > 0.004$ Å^{-1}, Fig. 3 indicates that the data follow a Q^{-4} Porod law, and the further changes in anisotropy seen in the *anisoscans* at larger Q must be attributed to the amplified anisotropy of the Porod scattering arising from the fine intralamellar cracks.

Comparison of Figs. 1(b) and (c) suggests that, as measured by their mean opening dimensions, the interlamellar pores have a broad size distribution, while the intralamellar cracks have a narrower size distribution with a finer mean size. Also, while significant fractions of both the interlamellar pores and intralamellar cracks are randomly distributed (see Table III), more interlamellar pores, overall, are aligned parallel with the substrate than intralamellar cracks are aligned perpendicular to it. This is particularly true for the coarse interlamellar pores. These observations are consistent both with previous work[18] and with the results of anisotropic structure modeling (next section), where two populations of interlamellar voids are needed in order to fit the scattering data.

In order to understand the effect of the process conditions and feedstock morphology on the structural anisotropy, scattering intensities from the *anisoscans* were plotted for PRM and POM specimens at three different Q values in Fig. 2, which shows only a modest variation in the scattering anisotropy among the PRM group specimens. This suggests that the depo-

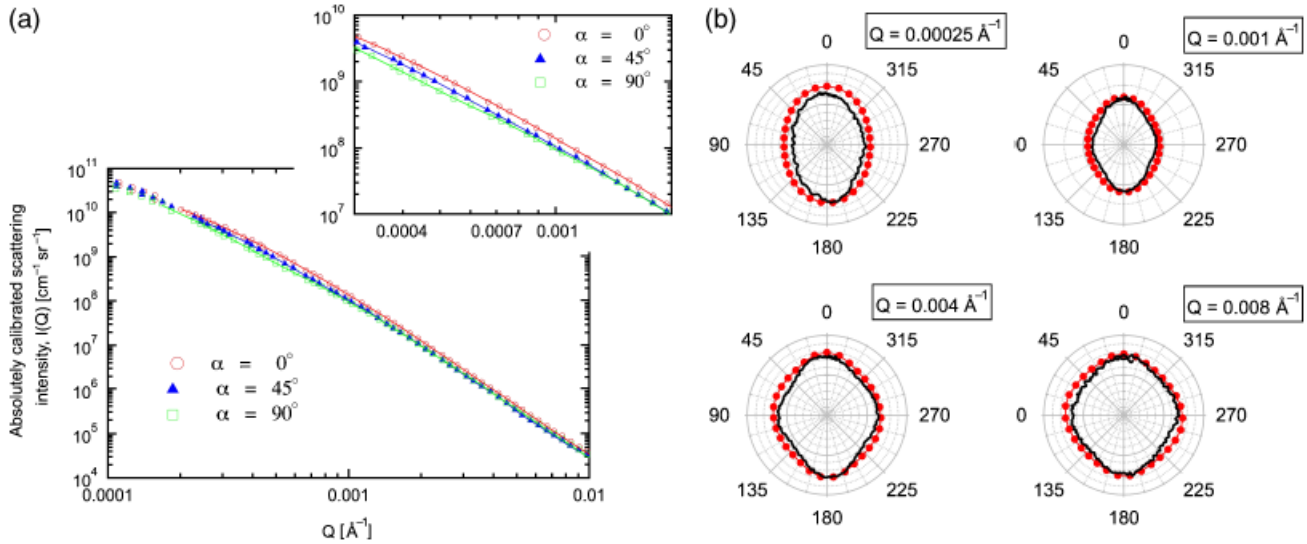

Fig. 3. Results for anisotropic ultrasmall-angle X-ray scattering structure refinement, containing data from three Q orientations; lines and symbols are the fitted and observed scattering intensities, respectively (left with inset showing detailed fits). The polar graphs (right) show the agreement between the calculated (filled circles) and observed (dark trace line) scattering anisotropy at four specified **Q** values.

Table III. Detailed Breakdown of the Void Components from Ultrasmall-Angle X-Ray Scattering (USAXS)

	Intralamellar cracks				Fine interlamellar pores				Coarse interlamellar pores				Globular pores	
Sample	⟨OD⟩ (μm)	Volume fraction (%)	Angular FWHM (deg.)	Random fraction	⟨OD⟩ (μm)	Volume fraction (%)	Angular FWHM (deg.)	Random fraction	⟨OD⟩ (μm)	Volume fraction (%)	Angular FWHM (deg.)	Random fraction	Diameter (μm)	Volume fraction (%)
PRM-1	0.020	0.51 (1)	120°	0.83	0.12	1.44 (1)	51°	0.87	0.45	3.48 (2)	67°	0.70	2.15	2.24 (2)
PRM-2	0.046	0.94 (1)	38°	0.93	0.15	3.61 (1)	26°	0.96	0.52	3.25 (2)	96°	0.63	2.40	1.09 (2)
PRM-3	0.041	0.67 (1)	30°	0.95	0.16	3.19 (2)	40°	0.88	0.51	4.38 (3)	56°	0.76	2.16	1.23 (2)
PRM-4	0.040	0.67 (1)	30°	0.97	0.15	3.40 (2)	35°	0.90	0.47	5.45 (3)	59°	0.68	1.78	1.56 (3)
POM–F&C	0.041	0.88 (1)	29°	0.94	0.15	4.09 (2)	18°	0.97	0.51	3.17 (3)	67°	0.73	2.38	2.07 (3)
POM–HOSP	0.036	0.78 (1)	120°	0.86	0.14	4.53 (2)	53°	0.82	0.40	5.56 (4)	73°	0.68	1.88	1.49 (2)
POM–A&S	0.042	0.55 (1)	75°	0.90	0.15	2.90 (2)	42°	0.95	0.41	4.31 (3)	45°	0.89	1.81	2.56 (3)

Fractional FWHM of size distributions: 0.2 for intralamellar cracks, 0.4 for both populations of interlamellar pores, 0.6 for globular pores. Aspect ratio, β: 0.1 for intralamellar cracks, 0.2 for both populations of interlamellar pores; 1.0 (spheres) for globular pores. Standard deviations given in parentheses in least significant digits for volume fractions; those for ⟨OD⟩ and diameters are about 1% of the value. Uncertainties for the FWHM of the angular range for preferred orientation, and for the population fraction that is randomly oriented, are discussed in the text. Uncertainty values given represent the constrained fit uncertainties. Microstructure processing and sampling uncertainties will be significantly larger. FWHM, full-width at half-maximum; POM, powder morphology; PRM, processing maps.

sition conditions, as used here, have only subtle effects on the microstructural anisotropy of F&C-derived coatings. However, significant variations in the scattering anisotropy are clearly observable among the POM group specimens. Thus, the microstructural anisotropy is more sensitive to feedstock morphology than to the processing conditions for a given feedstock. The relative increase, from HOSP to A&S to F&C, in the relative scattering intensity for the 90°–270° direction at all three Q values, is correlated with the microstructural anisotropy over the entire size range for the three feedstock coatings following the order: HOSP > A&S > F&C. Here, the scattering anisotropy is defined as the ratio of the *anisoscan* intensity in the 0°–180° azimuthal direction to that in the 90°–270° direction, and measures a mixture of the anisotropic orientation distributions of both the interlamellar pores and the intralamellar cracks, but is also reduced (increased) by a greater (lesser) relative prominence in the intralamellar crack population. With a significant crack population and discernibly different anisotropic distributions for the cracks and interlamellar pores, the crack component of the *anisoscan* is frequently distinguishable from the interlamellar pore component, particularly at high Q, due to the amplifying effect of the orientational anisotropy in the Porod scattering.[9–13] In the present case, the *anisoscans* indicate an anisotropic crack population that increases, relative to the other components, in the following order: HOSP < A&S < F&C. However, it should be noted that the *anisoscans* are self-normalized; so these trends do not necessarily reflect those in the absolute component volume fractions.

The USAXS anisotropy data are consistent with an earlier theoretical calculation that HOSP coatings exhibit the largest difference in thermal conductivity between the out-of-plane and in-plane directions.[18] This is not surprising because the HOSP feedstock produces a higher degree of flattening than other feedstocks. The fact that there are not larger differences in the thermal conductivities of most plasma-sprayed coatings in the two directions[18] indicates that the overall void population in the fine-scale regime (as measured with USAXS), which is less anisotropic than the coarse features (Fig. 1(c)) according to our definition above, has a greater impact than previously thought on the thermal conductivity of the coatings. Similarly, the microstructural anisotropy can be quantitatively related to the elastic modulus anisotropy, particularly for the POM samples where the variation of anisotropy is expected to be significant.

(2) Porosity of the PRM and POM Coatings

Small-angle scattering can arise from a variety of possible features such as, grain boundaries, second phases, pores, and interfaces. However, as the scattering contrast of the voids with respect to the solid splats is the largest among all of the microstructural features present, the scattering from pores dominates the overall scattering from porous plasma-sprayed YSZ coatings. The X-ray scattering contrast, $|\Delta\rho|^2$, is therefore determined by the square of the difference in the X-ray scattering-length (form-factor) density in the voids ($\rho = 0$) and in the YSZ ceramic, determined from the YSZ composition and mass density, together with standard X-ray form-factor data[39] ($\rho = 45.9 \times 10^{14}\ m^{-2}$). In order to quantify the microstructural characteristics, it was assumed[23] that each population of scatterers follows a Gaussian volume fraction size distribution with a fixed full-width at half-maximum (FWHM) and specific orientation distribution functions. The following assumptions were found to provide acceptable fits to the USAXS data for different **Q** orientations and also acceptable predictions of the *anisoscan* data: the FWHM of the intralamellar crack diameter distribution was set to 20% of the mean diameter, while that for each of the two interlamellar pore populations was set to 40% of their respective mean diameter, and the FWHM of the globular pore size distribution was set to 60% of the mean globular pore diameter. The orientation distribution functions assumed were as defined previously, with the parameter, a_1, set to 0° for the two populations of interlamellar pores, and to 90° for the intralamellar cracks. The parameters, a_2 and a_3, were adjusted to predict the observed *anisoscan* variations, and sometimes fitted to improve the model fits to the USAXS scan data. For both populations of interlamellar pores, and for the intralamellar cracks, only a relatively small fraction of each component is found to have the preferred orientation, while the rest is randomly oriented. However, the fraction of nonrandom oriented interlamellar pores is greater than for the intralamellar cracks, particularly for the coarse interlamellar pore population. Furthermore, the nonrandom distribution of interlamellar pores is more tightly aligned than it is for the intralamellar cracks.

Results for the fitted and derived parameters for each sample, using the anisotropic microstructure model described, are presented in Table III. For convenience, each anisotropic orientation distribution is given in terms of the randomly oriented fraction of the population, and the angular FWHM of the preferred orientation for the anisotropic part. Table III reveals a complex variation in the individual parameters for each pore population, but these combine to provide the trends described previously with respect to Figs. 1, 2, and 3. There is some covariance between the two orientation parameters presented in Table III for each population, making estimation of their individual uncertainties difficult to assess, but uncertainties in the pore dimensions and volume fractions are given in Table III. Typically, the interlamellar pores are distributed equitably between the fine and coarse populations with mean diameters ($2R_O$) of ≈1 and ≈3 μm, respectively. With $\beta = 0.2$, this implies corresponding mean ⟨OD⟩ values of 0.14 and 0.4 μm (smaller than the largest values discussed earlier). For the intralamellar cracks, typical mean diameters are obtained of ≈0.6 μm, implying that, with $\beta = 0.1$, the mean ⟨OD⟩ ≈ 40 nm. Meanwhile the mean globular void diameter was typically found to be ≈2

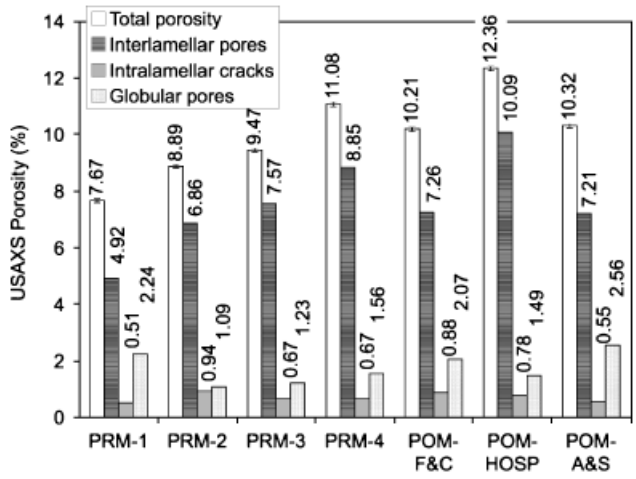

Fig. 4. Ultrasmall-angle X-ray scattering (USAXS)-derived total porosity and void component porosities for PRM and POM coatings obtained by anisotropic USAXS microstructural modeling.

μm. A typical outcome of the fitting is shown in Fig. 3. The three main components of the void structure and the total porosity for the PRM and POM specimens are then plotted in Fig. 4, where the two interlamellar pore populations, which define the TBC solid splat morphology, are summed together.

For all samples in this study, it was found that the interlamellar pores account for a major fraction of the total porosity (70%–80%). Previously, SANS, and specifically multiple small-angle neutron scattering (MSANS) has been used to quantify the three main void components in YSZ TBCs sprayed with different powder morphologies.[13–22] A lower fraction of interlamellar pores (30%–40%) was observed, although a similar level of total porosity was found compared with the current USAXS results. Table III indicates a possible explanation for this difference: the SANS/MSANS method may categorize much of the randomly oriented parts of the intralamellar crack and the two interlamellar pore populations as globular voids. Indeed, SANS smears out some of the anisotropic features in the coatings due to the larger sample volumes measured, and also the significant averaging over the angular width of the azimuthal sectors used. However, SEM studies indicate that the large-scale voids are mainly globular, and these may not be fully detected within the minimum Q limit for USAXS due to their size. It should be noted that there are few studies in the literature on the relationships among powder morphology, coating microstructure, and properties. It is indeed difficult to compare these results directly with other studies, as they have their own signature with respect to sources of feedstock and particle state. Based on a comparison of the porosity obtained from the USAXS structural model and from other measurements (precision density combined with SANS and MSANS) for a similar YSZ coating, Ilavsky *et al.*[23] found that the two approaches gave very close values for the sum of interlamellar pores and intralamellar cracks: however, USAXS gave less globular porosity (about 1% for USAXS versus 5.9% for SANS/MSANS) because the USAXS technique is mainly limited to sizes <1 μm. Conversely, the MSANS method does not have sufficient sensitivity to distinguish between the two populations of interlamellar pores and, as a result, may count some of the coarser population in with the globular pores.

(3) Relationship Between Processing, Microstructure, and Thermal Properties

As well as affecting the microstructural anisotropies among the PRM and POM samples, the feedstock morphology, together with the particle deposition temperature and velocity, plays an important role in determining the amounts of void component porosity in the resulting microstructure. A higher thermal or kinetic energy of the spray droplets usually results in stronger splat–splat interaction, consequently less porosity and an increased thermal conductivity. Indeed, Table I and Fig. 4 indicate that the total porosity increases from 8.9% to 11.1% with decreasing particle temperature and velocity (two parameters that are strongly correlated) for three PRM specimens (PRM-2, 3, and 4). Coatings PRM-1 and PRM-4 have similar particle deposition temperatures and velocities (Table I), but, based on the USAXS results (Table III and Fig. 4), they are dramatically different in both their component and total porosities. The one clear processing-related factor that distinguishes these two coatings is the H_2 flow rate in the plasma-forming gas (Table I), which was much less for PRM-1 than for PRM-4, and this could give rise to a change in the deposit morphology. When these data are evaluated together with the thermal conductivity data for all four PRM coatings, PRM-1 shows an anomaly in that PRM-1 and PRM-4 exhibit similar thermal conductivities, despite the differences in porosity and morphology. Based on the pore morphology PRM-1 would be expected to have a significantly greater thermal conductivity.

Two plausible explanations can address this issue:

Even though PRM-1 has similar average particle temperature and velocities, the effective melt content of PRM-1 can be substantially lower than that of PRM-4. The diagnostics only provide surface temperatures and not the melt content. In fact, PRM-1 has a lower melting index[4] than PRM-4. The consequence of this parametric difference is a significantly increased level of globular porosity within the coating (of PRM-1) as a result of entrapped *unmelted* particles and lack of adequate flattening. The USAXS results provide evidence of this, with almost 30% of the total porosity being globular for PRM-1 while this ratio is 12%–14% for the other three PRM samples. Note too that the total porosity as detected by USAXS is lowest for PRM-1. Therefore, it is possible that the diminished thermal conductivity of PRM-1 arises from its enhanced large-scale (globular) porosity.

Another possible explanation for the PRM-1 results may lie in a combination of a low gas pressure for H_2 (or possibly N_2) entrapped within the closed voids, arising from the low H_2 (or N_2) flow rates used in the spray-process for PRM-1, and the small $\langle \mathrm{OD} \rangle$ values found for the PRM-1 microstructure (Table III). The literature has shown how the thermal conductivity, K_{GAS}, of a low pressure gas confined within a fine pore (a Knudsen gas) can be significantly reduced from the thermal conductivity, $K_{\mathrm{O\_GAS}}$, of the same gas not so confined, and is of the form[40]:

$$K_{\mathrm{GAS}} = \frac{K_{\mathrm{O\_GAS}}}{\left(1 + \frac{BT}{\langle \mathrm{OD} \rangle P}\right)} \tag{7}$$

where T is the absolute temperature, P is the pressure, and B is a constant. Recently, the applicability of this relation to TBCs has been demonstrated.[41] For the PRM-1 coating, the $\langle \mathrm{OD} \rangle$ value, particularly for the intralamellar cracks, is small, and the flow rates for both the H_2 and N_2 spray gases are also small. Consequently, if the pressure, P, of any entrapped H_2 or N_2 gas is reduced, then K_{GAS} could be significantly reduced from $K_{\mathrm{O\_GAS}}$. A large number of fine cracks could act as a significant barrier to the heat flow, thus reducing the thermal conductivity measured. (Note that even though the conductivity was measured in the out-of-plane direction and the cracks are preferentially aligned perpendicular to the substrate, Table III indicates that some 83% of them are randomly aligned and will act as a barrier to heat transfer in any direction.)

The POM group specimens show similar porosities (10.2% and 10.3%, respectively) for coatings from the F&C and A&S feedstock, and higher porosity (12.7%) for coatings from the HOSP feedstock (Fig. 4), consistent with the lowest thermal conductivity being found for the HOSP coating (Fig. 5). The higher volume ratios of interlamellar pores to intralamellar cracks, combined with the low globular porosity found in the

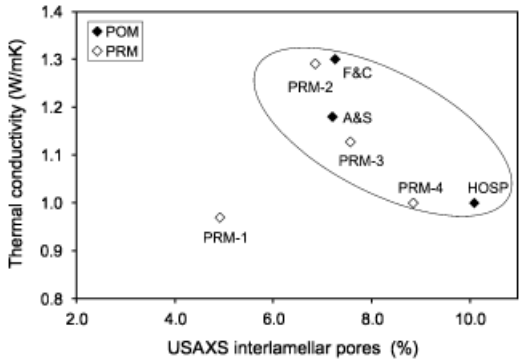

Fig. 5. Relationship between interlamellar porosity (USAXS) and through-thickness thermal conductivity for all seven specimens (both PRM and POM). USAXS, ultrasmall-angle X-ray scattering.

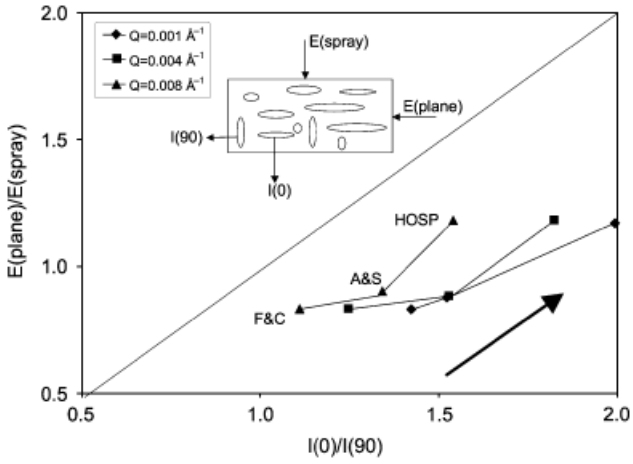

Fig. 6. Plot of the ratio of the indentation elastic moduli, E(plane)/E(spray) versus $I(0)/I(90)$ for three POM coatings, with an isoline corresponding to a state where the two ratios are equal.

HOSP coatings, result in the strong structural anisotropy of the POM–HOSP specimen, as defined with respect to the *anisoscan* plots, discussed earlier.

When the measured thermal conductivities are plotted against each void component, as well as the total porosity obtained from the USAXS data analysis for corresponding specimens, a correlation is found only for the interlamellar pores and the total porosity, except for the PRM-1 specimen (Fig. 5). The relationship between porosity and thermal conductivity is similar for the PRM and POM coatings (excluding PRM-1). Although all types of pores can play specific roles in impeding heat flow, it is usually the interlamellar pores that contribute most effectively to impeding the heat flow through the thickness. Linear fits of the thermal conductivity versus the total porosity for the data found for six of the coatings give an extrapolation to a thermal conductivity of 2.0 $W \cdot (m \cdot K)^{-1}$ at zero porosity, acceptably close to the ideal value of 2.2–2.9 $W \cdot (m \cdot K)^{-1}$ reported for fully dense tetragonal YSZ ceramics.[42] The difference can be justified by additional coarse porosity (mostly in the form of globular pores) that are present, but not identified by USAXS, or by the possible presence of a minor secondary phase (i.e., monoclinic, cubic YSZ) in the coatings, as suggested in the literature.[43]

(4) Relationship Between USAXS-Derived Microstructure and Elastic Modulus in POM Coatings

Table II presents results for the elastic modulus measured by the indentation method for both the in-plane and out-of-plane (spray) directions. The different values for the two directions, exhibited in the plasma-sprayed POM coatings, imply a mechanical anisotropy associated with that of the underlying porosity in the microstructure, as reported for similar coatings by other authors.[44,45] We define the indentation elastic modulus anisotropy coefficient as: E(plane)/E(spray). Compared with an elastic modulus of about 200 GPa for dense zirconia, the reduction in elastic modulus is attributable to the pore and crack morphology. As noted in Table II, E(spray) can be less than or greater than E(plane). Typically $E(\text{plane})/E(\text{spray}) > 1$ is expected, as plasma-sprayed coatings normally have their interlamellar pores, oriented predominantly parallel to the substrates, giving the most significant reduction in elastic modulus in the spray direction. That is the case for the HOSP coating. However, it is not unusual to find inverse anisotropy [$E(\text{plane})/E(\text{spray}) < 1$],[46] as exhibited by the F&C and A&S coatings.

The small-angle scattering intensities at $\alpha = 0^\circ$ and 90° (denoted $I(0)$ and $I(90)$) are related to the surface area and volume fraction of the voids within the YSZ matrix that are predominantly parallel or perpendicular, respectively, to the substrate. Indeed, the ratio, $I(0)/I(90)$, may be used as a form of microstructural anisotropy coefficient. Figure 6 is a plot of the elastic modulus anisotropy versus this microstructure anisotropy coefficient. The elastic modulus anisotropy of the coatings depends not only on the interlamellar void and intralamellar crack porosities, but also on their orientation distributions.[44,47] The strong correlation between the two anisotropy ratios (Fig. 6) at three different Q values indicates that it is when the plane of the interlamellar pores or intralamellar cracks is perpendicular to the elastic modulus measurement direction (Fig. 6, inset) that the coatings have the greatest compliance, and hence the greatest reduction in elastic modulus. Here, the largest value of E(plane)/E(spray) was found for the HOSP coating, consistent with a significant large volume fraction of interlamellar pores (Table III and Fig. 4). The F&C and A&S coatings showed a reverse elastic modulus anisotropy, underlining the fact that the multicomponent model must be used to interpret the USAXS intensity anisotropy in terms of the relative prominence, size, and orientation distributions of the two population of interlamellar pores and the intralamellar crack population (this two population distribution was necessitated from the mathematical model used here). Overall, the results presented here, aimed at correlating the TBC microstructure with the elastic modulus anisotropy, are broadly consistent with those of a previous MSANS study.[13] In principle, USAXS studies can go further than can analysis of the copious multiple scattering in MSANS. This is because (after modest multiple scattering correction of the USAXS data) single scattering theory can be applied to the whole scale range of interest from a few tens of nanometers up to more than a micrometer.

Elastic moduli were not measured for the PRM series. Inasmuch as the particle temperature and velocity are not mutually independent, an interpretation of the results would have been of doubtful significance. In fact, it is likely that other process variables such as carrier gas pressure and type should be considered in developing a process map defined by totally independent variables. Therefore, we defer further discussion of elastic moduli until additional experiments and analysis have verified the mutual independence of the map variables.

IV. Conclusions

USAXS studies have enabled the complex, anisotropic, multicomponent microstructures of TBCs to be characterized and quantified to an unprecedented degree, and have revealed that two populations of interlamellar pores, as well as a population of intralamellar cracks and a coarse globular pore population, are required to describe the TBC splat/void morphology. For a set of samples that have been sprayed and fabricated under a well-instrumented level of process control, the USAXS studies have yielded the following conclusions:

(1) The complex pore network components within TBC materials can be quantified to a new level of detail by USAXS

analysis using a multicomponent anisotropic model using Gaussian size distributions that can be implemented for a range of TBC microstructures.

(2) The elastic modulus anisotropy for coatings with different powder morphologies correlates well with the corresponding microstructural anisotropy determined by USAXS. More importantly, USAXS can relate property anisotropy, quantitatively, to the underlying void component anisotropies.

(3) An exception to the processing–microstructure–property relationships and trends, more universally observed, can occur when a combination of the processing conditions results in a particularly fine pore or crack network together with a presumed low entrapped gas pressure. Under these circumstances, Knudsen gas transport conditions can apply, resulting in a significant lowering of the thermal conductivity. Because this is frequently a desired TBC property, investigation of the circumstances that bring this situation about should be a subject of future research. Measurements of the thermal conductivity in different atmospheres (and perhaps at elevated temperatures) could identify the entrapped gas species, quantify the fraction of fine voids that are closed, and determine to what extent the "Knudsen gas" case could be exploited to lower TBC thermal conductivity.

More broadly, this study illustrates how TBC microstructure information is particularly valuable when it can be related to well-characterized and controlled processing conditions and feedstock morphologies, as well as to variations in the physical properties of the coatings. This will lead to new perspectives on the development of advanced TBCs, particularly when combined with the process maps currently being developed for plasma-sprayed TBCs.[30]

Acknowledgment

We are grateful to Brian Choi of the Center of Thermal Spray Research at Stony Brook for providing the elastic modulus data, and to Edwin Fuller Jr. of NIST Ceramics Division for valuable discussion of the Knudsen gas effect.

References

[1]R. Vaβen, N. Czech, W. Mallener, W. Stamm, and D. Stover, "Influence of Impurity Content and Porosity of Plasma-Sprayed Yttria-Stabilized Zirconia Layers on the Sintering Behavior," *Surf. Coat. Technol.*, **141**, 135–40 (2001).

[2]H. Guo, S. Kuroda, and H. Murakami, "Microstructures and Properties of Plasma-Sprayed Segmented Thermal Barrier Coatings," *J. Am. Ceram. Soc.*, **89**, 1432–9 (2006).

[3]N. P. Padture, K. W. Schlichting, T. Bhatia, A. Ozturk, R. Cetegen, E. H. Jordan, M. Gell, S. Jiang, T. D. Xiao, P. R. Strutt, E. Garcia, P. Miranzo, and M. I. Osendi, "Towards Durable Thermal Barrier Coatings with Novel Microstructures Deposited by Solution-Precursor Plasma Spray," *Acta Mater.*, **49**, 2251–7 (2001).

[4]S. Sampath, X. Y. Jiang, J. Matejicek, L. Prchlik, A. Kulakarni, and A. Vaidya, "Role of Thermal Spray Processing Method on the Microstructure, Residual Stress and Properties of Coatings: An Integrated Study for Ni–5wt%Al Bond Coats," *Mater. Sci. Eng. A*, **364**, 216–31 (2004).

[5]A. J. Allen, "Characterization of Ceramics by X-ray and Neutron Small-Angle Scattering," *J. Am. Ceram. Soc.*, **88**, 1367–81 (2005).

[6]D. W. Schaefer and M. M. Agamalian, "Ultra-Small-Angle Neutron Scattering: A New Tool for Materials Research," *Curr. Opin. Solid State Mater. Sci.*, **8**, 39–47 (2004).

[7]K. Hardman-Rhyne, N. F. Berk, and E. R. Fuller, "Microstructural Characterization of Ceramic Materials by Small-Angle Neutron Scattering Techniques," *J. Res. Nat. Bur. Stand.*, **89**, 17–34 (1984).

[8]A. J. Allen and N. F. Berk, "Analysis of Small-Angle Scattering Data Dominated by Multiple Scattering for Systems Containing Eccentrically Shaped Particles or Pores," *J. Appl. Cryst.*, **27**, 878–91 (1994).

[9]J. Ilavsky, A. J. Allen, G. G. Long, S. Krueger, C. C. Berndt, and H. Herman, "Influence of Spray Angle on the Porous Microstructure of Plasma-Sprayed Ceramic Deposits," *J. Am. Ceram. Soc.*, **80**, 733–42 (1997).

[10]J. Ilavsky, A. J. Allen, G. G. Long, H. Herman, and C. C. Berndt, "Characterization of the Closed Porosity in Plasma-Sprayed Alumina," *J. Mater. Sci.*, **32**, 3407–10 (1997).

[11]J. Ilavsky, G. G. Long, A. J. Allen, M. Prystay, and C. Moreau, "Anisotropic Microstructure of Plasma-Sprayed Deposits," *J. Thermal Spray Technol.*, **8**, 414–20 (1999).

[12]J. Ilavsky, G. G. Long, A. J. Allen, and C. C. Berndt, "Evolution of the Void Structure in Plasma-Sprayed YSZ Deposits During Annealing," *Mater. Sci. Eng. A*, **272**, 215–21 (1999).

[13]A. J. Allen, J. Ilavsky, G. G. Long, J. Wallace, C. C. Berndt, and H. Herman, "Microstructural Characterization of Yttria-Stabilized Zirconia Plasma-Sprayed Deposits Using Multiple Small-Angle Neutron Scattering," *Acta Mater.*, **49**, 1661–75 (2001).

[14]A. J. Allen, G. G. Long, H. Boukari, J. Ilavsky, A. Kulkarni, S. Sampath, H. Herman, and A. N. Goland, "Microstructural Characterization Studies to Relate the Properties of Thermal Spray Coatings to Feedstock and Spray Conditions," *Surf. Coatings Technol.*, **146–147**, 544–52 (2001).

[15]A. J. Allen, N. F. Berk, J. Ilavsky, and G. G. Long, "Multiple Small-Angle Neutron Scattering Studies of Anisotropic Materials," *Appl. Phys. A*, **74** [Suppl.] S937–9 (2002).

[16]T. Keller, W. Wagner, A. J. Allen, J. Ilavsky, N. Margadant, S. Siegmann, and G. Kostorz, "Characterization of Thermally-Sprayed Metallic NiCrAlY Deposits by Multiple Small-Angle Scattering," *Appl. Phys. A*, **74** [Suppl.] S975–7 (2002).

[17]H. Boukari, A. J. Allen, G. G. Long, J. Ilavsky, J. Wallace, C. C. Berndt, and H. Herman, "Small-Angle Neutron Scattering Study of the Role of Feedstock Particle Size on the Microstructural Behavior of Plasma-Sprayed YSZ Deposits," *J. Mater. Res.*, **18**, 624–34 (2003).

[18]A. Kulkarni, Z. Wang, T. Nakamura, S. Sampath, A. Goland, H. Herman, J. Allen, J. Ilavsky, G. Long, J. Frahm, and R. W. Steinbrech, "Comprehensive Microstructural Characterization and Predictive Property Modeling of Plasma-Sprayed Zirconia Coatings," *Acta Mater.*, **51**, 2457–75 (2003).

[19]T. A. Dobbins, A. J. Allen, J. Ilavsky, G. G. Long, A. Kulkarni, H. Herman, and P. R. Jemian, "Recent Developments in the Characterization of Anisotropic Void Populations in Thermal Barrier Coatings Using Ultra-Small-Angle X-Ray Scattering"; pp. 517–24, *27th International Cocoa Beach Conference on Advanced Ceramics and Composites*: A, 24, American Ceramic Society, 2003.

[20]A. Kulkarni, A. Goland, H. Herman, A. J. Allen, J. Ilavsky, G. G. Long, C. A. Johnson, and J. A. Ruud, "Microstructure–Property Correlations in Industrial Thermal Barrier Coatings," *J. Am. Ceram. Soc.*, **87**, 1294–300 (2004).

[21]A. A. Kulkarni, A. Goland, H. Herman, A. J. Allen, J. Ilavsky, G. G. Long, and F. De Carlo, "Advanced Microstructural Characterization of Plasma-Sprayed Zirconia Coatings Over Extended Length Scales," *J. Thermal Spray Technol.*, **14**, 239–50 (2005).

[22]A. A. Kulkarni, S. Sampath, A. Goland, H. Herman, A. J. Allen, J. Ilavsky, W. Q. Gong, and S. Gopalan, "Plasma Spray Coatings for Producing Next-Generation Supported Membranes," *Topics Catal.* **32**, 241–9 (2005).

[23]J. Ilavsky, A. J. Allen, T. Dobbins, A. Kulkarni, and H. Herman, "Microstructure Characterization of Thermal Barrier Coating Deposits—Practical Models from Measurements"; pp. 1318–23 in *Proceedings of the International Thermal Spray Conference*, Basel, Switzerland, May 2–4, 2005

[24]A. Kulkarni, J. Gutleber, S. Sampath, A. Goland, W. B. Lindquist, H. Herman, A. J. Allen, and B. Dowd, "Studies of the Microstructure and Properties of Dense Ceramic Coatings Produced by High-Velocity Oxygen-Fuel Combustion Spraying," *Mater. Sci. Eng. A*, **369**, 124–37 (2004).

[25]A. A. Kulkarni, H. Herman, J. Almer, U. Lienert, D. Haeffner, J. Ilavsky, S. Fang, and P. Lawton, "Depth-Resolved Porosity Investigation of EB-PVD Thermal Barrier Coatings Using High-Energy X-Rays," *J. Am. Ceram. Soc.*, **87**, 268–74 (2004).

[26]A. Kulkarni, A. Goland, H. Herman, A. J. Allen, T. Dobbins, F. De Carlo, J. Ilavsky, G. G. Long, S. Fang, and P. Lawton, "Advanced Neutron and X-ray Techniques for Insights into the Microstructure of EB-PVD Thermal Barrier Coatings," *Mater. Sci. Eng. A*, **426**, 43–52 (2006).

[27]A. Flores Renteria, B. Saruhan, J. Ilavsky, and A. J. Allen, "Application of USAXS Analysis and Non-Interacting Approximation to Determine the Influence of Process Parameters and Ageing on the Thermal Conductivity of Electron-Beam Physical Vapor Deposited Thermal Barrier Coatings," *Surf. Coat. Technol.*, **201**, 4781–8 (2007).

[28]J. Ilavsky, A. J. Allen, G. G. Long, and P. R. Jemian, "Effective Pinhole-Collimated Ultrasmall-Angle X-Ray Scattering Instrument for Measuring Anisotropic Microstructures," *Rev. Sci. Instrum.*, **73**, 1660–2 (2002).

[29]J. A. Potton, G. J. Daniell, and B. D. Rainford, "Particle-Size Distributions from SANS Data Using the Maximum-Entropy Method," *J. Appl. Cryst.*, **21**, 663–8 (1988).

[30]A. Vaidya, V. Srinivasan, T. Streibl, M. Friis, W. Chi, and S. Sampath, "Process Maps for Plasma Spraying of Yttria Stabilized Zirconia: An Integrated Approach to Design, Optimization and Reliability," *Mater. Sci. Eng. A*, **497**, 239–53 (2008).

[31]Y. Liu, T. Nakamura, V. Srinivasan, A. Vaidya, A. Gouldstone, and S. Sampath, "Nonlinear Elastic Properties of Plasma Sprayed Zirconia Coatings and Associated Relationships to Processing Conditions," *Acta Mater.*, **55**, 4667–78 (2007).

[32]G. Porod, "General Theory"; pp. 17–51 in *Small-Angle X-ray Scattering*, Edited by O. Glatter, and O. Kratky. Academic Press, London, 1982.

[33]G. G. Long, A. J. Allen, J. Ilavsky, P. R. Jemian, and P. Zschack, "The Ultra-Small Angle X-ray Scattering Instrument on UNICAT at the APS"; pp. 183–7 in *Synchrotron Radiation Instrumentation: Eleventh U.S. National Conference*, Edited by P. Pianetta, J. Arthur, and S. Brennan. AIP Melville, New York, 2000.

[34]J. Ilavsky, P. R. Jemian, A. J. Allen, and G. G. Long, "Versatile USAXS (Bonse-Hart) Facility for Advanced Materials Research," *AIP Conf. Proc.*, **705**, 510–3 (2004).

[35]Indra2: http://www.uni.aps.anl.gov/~ilavsky/indra_2.html

[36]W. A. Dollase, "Correction of Intensities for Preferred Orientation in Powder Diffractometry—Application of the March Model," *J. Appl. Crystallogr.*, **19**, 267–72 (1986).

[37]W. Chi, S. Sampath, and H. Wang, "Microstructure–Thermal Conductivity Relationships in Plasma Sprayed Yttria Stabilized Zirconia," *J. Am. Ceram. Soc.*, **91** [8] 2636–45 (2008).

[38]W. Chi, S. Sampath, and H. Wang, "Ambient and High-Temperature Thermal Conductivity of Thermal Spray Coatings," *J. Thermal Spray Technol.*, **15** [4] 773–8 (2006).

[39]C. T. Chantler, K. Olsen, R. A. Dragoset, J. Chang, A. R. Kishore, S. A. Kotochigova, and D. S. Zucker, *X-ray Form Factor, Attenuation and Scattering Tables (version 2. 1)*. National Institute of Standards and Technology, Gaithersburg, MD, 2005. Available online at: http://physics.nist.gov/ffast.

[40]I. O. Golosnoy, S. A. Tsipas, and T. W. Clyne, "An Analytical Model for Simulation of Heat Flow in Plasma-Sprayed Thermal Barrier Coatings," *J. Thermal Spray Technol.*, **14**, 205–14 (2005).

[41]A. D. Jadhav, N. P. Padture, E. H. Jordan, M. Gell, P. Miranzo, and E. R. Fuller Jr., "Low-Thermal-Conductivity Plasma-Sprayed Thermal Barrier Coatings with Engineered Microstructures," *Acta Mater.*, **54**, 3343–9 (2006).

[42]L. Pawlowski and P. Fauchais, "Thermal Transport Properties of Thermally Sprayed Coating," *Int. Mater. Rev.*, **37**, 271–90 (1992).

[43]J. Ilavsky and J. K. Stalick, "Phase Composition and Its Changes During Annealing of Plasma-Sprayed YSZ," *Surf. Coat. Technol.*, **127**, 120–9 (2001).

[44]H. Kim and Y. Kweon, "Elastic Modulus of Plasma-Sprayed Coatings Determined by Indentation and Bend Tests," *Thin Solid Film*, **342**, 201–6 (1999).

[45]Z. Wang, A. Kulkarni, S. Deshpande, T. Nakamura, and H. Herman, "Effects of Pores and Interfaces on Effective Properties of Plasma-Sprayed Zirconia Coatings," *Acta Mater.*, **51**, 5319–34 (2003).

[46]I. Sevostianov and M. Kachanov, "Modeling of the Anisotropic Elastic Properties of Plasma-Sprayed Coatings in Relation to Their Microstructure," *Acta Mater.*, **48**, 1361–70 (2000).

[47]H. Nakahira, K. Tanl, K. Miyajima, and Y. Harada, "Anisotropy of Thermally Sprayed Coatings"; pp. 1011–7 in *Proceedings of the International Thermal Spray Conference & Exposition*, Orlando, FL, May 28 to June 5, 1992. □